Composites Part B 230 (2022) 109487

Contents lists available at ScienceDirect

Composites Part B

journal homepage: www.elsevier.com/locate/compositesb

Next-generation Li-ion capacitor with high energy and high power by limiting alloying-intercalation process using SnO_2@Graphite composite as battery type electrode

Madhusoodhanan Lathika Divya [a], Selvarasu Praneetha [a], Yun-Sung Lee [b], Vanchiappan Aravindan [a,*]

[a] Department of Chemistry, Indian Institute of Science Education and Research (IISER) Tirupati, 517507, India
[b] School of Chemical Engineering, Chonnam National University, Gwang-ju, 61186, Republic of Korea

ARTICLE INFO

Keywords:
Lithium-ion capacitors
SnO_2@Graphite nanocomposites
High energy-high power LIC
Alloying
Intercalation

ABSTRACT

Lithium-ion capacitors (LICs) with high energy density at high power capability are ideal for future energy storage applications. Group IV elements, mainly tin (Sn)-based derivatives, are considered as a viable option due to their high reversible capacity, lower redox potential, and moderately lower price. In the present work, we report the assembly of a new type of LIC with high energy and power with long-term stability by pairing SnO_2@Graphite nanocomposites (SnO_2@G *ncs*) as battery type electrodes and commercial activated carbon (AC) as capacitor type electrodes. SnO_2@G *ncs* are synthesized by hydrothermal method followed by high-energy ball milling of SnO_2 and commercial graphite. The testing potential window of the SnO_2 @G *ncs* half–cells are limited to 1 V *vs.* Li^+/Li to enable only the alloying process and avoid the conversion of Sn^0 to SnO_x. Among the compositions, the composite with 25% SnO_2 and 75% graphite (C_1)-based LIC, AC/C_1 displayed stable performance with high energy and power. Furthermore, AC/C_1-based LIC delivers an energy density of 172.33 Wh kg^{-1} and retains over 90% capacity after 9000 cycles. This study gives the idea of incorporating an alloying-intercalation-based battery-type electrode, which paves the way further to enhance the electrochemical performance of next-generation LICs.

1. Introduction

In the present age, Lithium-ion batteries (LIBs) and Supercapacitors are the two effective electrochemical energy storage technologies with complementary performance features mainly due to the difference in the charge storage mechanism [1–6]. LIBs, having wide application in portable electronics and electric vehicle (EV) technology, can deliver high energy density (130–200 Wh kg^{-1}) along with a low self-discharge rate. However, low power density (<1000 W kg^{-1}) and short cycle life (<1000 cycles) are due to diffusion-limited Faradaic reactions and greater polarization [7–11]. In contrast, electric double-layer capacitors (EDLCs) can exhibit power density values up to 10 kW kg^{-1} along with long cycle life but with limited specific energy values (<5 Wh kg^{-1}) and a high self-discharge rate [12,13]. The goal of achieving a single system with high energy and power combined with long cycle life brought the idea of merging the positive qualities of LIBs and EDLCs to construct a battery supercapacitor hybrid energy storage system, named as Lithium-ion capacitor (LICs) [14–16]. LICs generally hire an EDLC electrode as the cathode that can provide high power, and high energy is supplemented by LIB electrode as the anode in the presence of Li salt-containing organic electrolyte [17]. The use of LICs is steadily mounting as they aid in compensating varying voltage levels with solar panels, serve as a backup solution for power interruption in servers and other devices [18,19]. Moreover, LICs can be considered logically safe as EDLC devices, as they will not cause serious thermal runaway due to differences in positive electrode material compared with LIBs [20–23].

The performance of LIC primarily depends on the nature of electroactive materials (electrodes and electrolytes) and the electrode configuration in the device. Dual-carbon LICs (DC-LICs), having carbon-based electrodes as battery and capacitive type electrodes, has gained significant attention owing to environmental concern and cost-effectiveness [24–26]. However, the energy density of such LICs is inadequate to drive all those mentioned above and the newly emerging applications, which is mainly due to limited Li-ion diffusion kinetics of battery-type

* Corresponding author.
E-mail addresses: aravind_van@yahoo.com, aravindan@iisertirupati.ac.in (V. Aravindan).

https://doi.org/10.1016/j.compositesb.2021.109487
Received 11 October 2021; Received in revised form 3 November 2021; Accepted 14 November 2021
Available online 18 November 2021

electrodes (graphite and hard carbon). Moreover, the graphite anodes (theoretical capacity of 372 mAh g^{-1}, and low intercalation potential, <0.1 V *vs.* Li^+/Li) suffer a serious problem of Li platting while operating at high current rates; thus, they cannot be used for EV and Hybrid EV applications. This triggered the research on electrode materials for new generation LICs with high energy density, which is only possible by altering the battery type electrode as changes in the supercapacitor component (activated carbon, AC) are highly constrained due to its adsorption-desorption type charge-storage mechanism. Active materials that can electrochemically alloy with Li have become the most viable option as they have high reversible specific capacities and low reduction potentials. Among them, tin oxide (SnO_2) is one of the most hopeful anode candidates for next-generation Li-based energy storage devices due to its high theoretical Li-storage capacity of 1494 mAh g^{-1}, low redox potential (~0.3 V *vs.* Li^+/Li), environmental friendliness, low cost, and natural abundance [27–29]. The Li-storage mechanism in SnO_2 is a two-step reaction: the combination of conversion reaction and alloying-dealloying reaction [30,31].

$$SnO_2 + 4Li^+ + 4e^- \leftrightarrow Sn^0 + 2Li_2O \quad (1)$$

$$Sn^0 + xLi^+ + xe^- \leftrightarrow Li_xSn \quad (0 < x \leq 4.4) \quad (2)$$

The SnO_2 material is first converted into tin metal (Sn^0) and lithium oxide (Li_2O) (1), and then there is a reversible alloying reaction (2). Equation (1) is considered irreversible and consumes a substantial amount of Li-ions to form Li_2O, serving as a mechanical buffer against significant volume change during the de-lithiation step. The main drawbacks of SnO_2 based anode material are pulverization and coarsening of particles during cycling due to volume expansion (~259% for crystalline and ~305% for amorphous) and rapid capacity fading due to unstable solid electrolyte interface (SEI) formation [32]. Nevertheless, this can be effectively controlled by creating nanostructured morphology with voids, preparing carbon composites, and also limiting the test potential window [33].

Developing high-performance LICs is a real challenge due to the imbalance in the energy storage capacity and power capability between the two electrodes. As part of optimizing a suitable anode-cathode combination, several LICs have been reported with progressive performances. The LIC system with SnO_2–C hybrid anode (SnO_2–C/C) was first stated by Qu et al. [34]. Later in 2016, Sun et al. [35] assembled a LIC by integrating Sn–C anode and biomass-derived microporous activated carbon cathode. Pre-treated SnO_2 nanorods bundle as the negative electrode in combination with jackfruit skin-derived AC as cathode, Sennu et al. [36] reported SnO_2/JF-AC-based LIC assembly. Recently, ultra-thin carbon layer coated porous SnO_2 as anode and commercial activated carbon as cathode, SnO_2@C/AC (YP–80F) LIC, was fabricated by Tran et al. [37], using reduced graphene oxide decorated with SnO_2 nanoparticles as the negative electrode and olive pits derived AC as the cathode. Arnaiz et al. [38] developed SnO_2-rGO/AC-based LIC. Despite those studies, there is still a research requirement to explore new LIC configurations with high energy and power density and cyclic stability by eliminating kinetic mismatch and capacity divergence between the two electrodes. Also, all the studies with SnO_2 were reported with alloying/or conversion reaction only, in which conversion process leads to the increase in the polarization that results in dilution of the energy. Apparently, the purpose of using carbonaceous materials (coating or composite) is mainly to sustain the volume variation and not indented for the reversible charge-storage (e.g., intercalation) [39]. However, to date, there is no systematic study has been reported on limiting Sn–C composite to study the simultaneous evolution of both alloying and insertion processes for highly efficient and reversible Li-storage towards the development of next-generation charge storage devices.

In this study, we have prepared SnO_2@G *ncs* by mechanical milling of hydrothermally prepared SnO_2 and commercial graphite in various proportions (Table S1). The testing potential window was limited to enable the alloying-intercalation process only [28]. We also report the assembly of a new LIC configuration by combining pre-lithiated SnO_2@G *ncs* as battery type electrode (LiC_6 & Li_xSn) and commercial AC as the capacitive electrode under the balanced conditions. The performance of composite LICs was compared with LICs having ball-milled samples of SnO_2 and commercial graphite as the battery-type negative electrode. Further, the composite LIC having a superior performance at ambient conditions was also tested at high and low-temperature conditions and discussed in detail.

2. Experimental procedure

2.1. SnO_2 synthesis

In a typical preparation, 2 M of NaOH aqueous solution was added dropwise into 15 mL of water and 5 mL of ethanol containing 10 mmol of $SnCl_2.2H_2O$. The pH was adjusted until it reached 13. The obtained white turbid mixture was transferred into a 100 mL Teflon-lined autoclave, sealed and maintained at 180 °C for 24 h, and then cooled to room temperature. The obtained precipitates were washed several times with water and ethanol, respectively. The final product dried under vacuum at 75 °C overnight and was subjected to further studies.

2.2. SnO_2@Graphite nanocomposite preparation

SnO_2@Graphite nanocomposites were prepared by mixing different mass ratios of hydrothermally synthesized SnO_2 material with commercial graphite powder and ball milled in high energy planetary ball mill for 30 min with the ball to powder weight ratio of 20:1. The Amount of Graphite and SnO_2 were adjusted to make 5 different compositions (100:0, 75:25, 50:50, 25:75, and 0:100) of active electrode material and were named as Graphite–BM, C_1, C_2, C_3, and SnO_2−BM, Table S1.

2.3. Material characterization

The X-ray diffraction (XRD) measurements were carried out on a Rigaku D/teX Ultra 250 diffractometer using Cu Kα radiation (40 kV, 200 mA, λ = 1.5406 Å). Raman spectroscopy was examined with Lab-Ram HR800 UV Raman microscope (Horiba Jobin-Yvon, France) with 515 nm Diode laser as excitation light source. The surface functional groups and heteroatoms on the material surface were analyzed by X-ray photoelectron spectroscopy (XPS, Multilab 2000, UK; monochromatic Al Kα radiation hν = 1486.6 eV). Structural investigation of the SnO_2 graphite nanocomposite was done with scanning electron microscopy (SEM S-4700, Hitachi, Japan), Energy-dispersive spectroscopy (EDS), and High-resolution Transmission electron microscopy (HR-TEM, TECNAI, Philips, the Netherlands, 200 keV).

2.4. Electrochemical performance analysis

SnO_2@Graphite nanocomposites, SnO_2@G *ncs* (C_1, C_2, and C_3), Graphite BM, SnO_2−BM and commercial AC, (YP 80F Kuraray, Japan; Surface area: 2100 m^2 g^{-1}, Pore volume: 0.97 mL g^{-1}) were first tested as a negative and positive electrode active material in half-cell configuration using Li metal foil as the counter electrode. The SnO_2@G *ncs*, Graphite BM, and SnO_2−BM negative electrodes were fabricated using a typical slurry coating method, in which SnO_2@G *nc* active materials, conductive carbon black, and polyvinylidene fluoride (PVdF) binder were dissolved in the *N*-methyl-2-pyrrolidinone (NMP) with the mass ratio of 70:20:10. The slurry coated (MSK-AFA-III Automatic Thick Film Coater (MTI Corporation) Cu foils were dried and pressed under a hot roll press (Tester Sangyo, Japan). 14 mm diameter electrodes were punched with mass loading of ~1–2 mg active material and were dried at 75 °C under vacuum for 4 h. AC based positive electrodes were prepared by mixing the activated carbon, conductive carbon black, and teflonized acetylene black (TAB-2) binder in the weight ratio of 80:10:10 using ethanol as solvent and was pressed on a 14 mm diameter stainless

steel mesh current collector (Goodfellow, UK) and were also dried at 75 °C under vacuum for 4 h. Further, the half–cells were fabricated in an Ar-filled glovebox using Whatman paper (1825–047, GF/F) as separator and 1 M $LiPF_6$ in ethylene carbonate (EC): dimethyl carbonate (DMC), 1:1 v/v, Tomiyama, Japan as electrolyte (125–150 μl). The AC/SnO_2@G *ncs* hybrid capacitors were assembled by coupling a pre-lithiated SnO_2@G *nc* electrode (LiC_6 & Li_xSn) as the negative electrode (2 complete discharge-charge cycles followed by third discharge ending at 0.005 V *vs*. Li^+/Li, representing the lithiated state) and a fresh AC electrodes positive electrode. The mass ratios of AC to SnO_2@G *ncs* were adjusted based on the half–cell performance and were approximately 3.5:1 for Graphite BM, 4:1 for C_1, 5:1 for C_2, 6:1 for C_3, and 7:1 for SnO_2 BM material.

The electrochemical performance of half-cells and hybrid capacitor configurations were studied in CR 2016 coin−cell assembly. Galvanostatic charge-discharge (GCD), cyclic voltammetry (CV), and Electrochemical Impedance spectrometry (EIS) studies were done by a Battery tester (Biologic, France). The SnO_2@G *ncs* and AC electrode voltage windows were fixed as 0.005–1 V and 2–4.5 V *vs*. Li^+/Li. The GCD of AC/SnO_2@G *ncs* hybrid capacitors were tested within the potential window of 1.7–4.2 V. The EIS study was done within the frequency range of 10 kHz to 10 mHz at an amplitude of 10 mV. The energy and power density values of the assembled LICs were calculated using standard equations (given in supplementary) based on the total mass of active material present in both electrodes. The low and high-temperature performance of assembled LIC was studied with the help of an environmental chamber (Espec, Japan).

3. Results and discussion

The phase purity and crystalline structure of ball-milled samples of commercial graphite (graphite -BM), hydrothermally synthesized and subsequently ball-milled SnO_2 (SnO_2–BM), and SnO_2@Graphite nanocomposites (C_1, C_2 & C_3) were investigated by powder X-ray diffraction (XRD) measurements (Fig. 1a & Fig. S1). All the peaks in the XRD pattern of Graphite–BM can be indexed to hexagonal graphite 2H, syn with space group $P6_3/mmc$; ICDD (PDF-2+2019 RDB) 00-056-0160, $a = b = 2.46$ Å, and c = 6.707 Å). The crystal structure of the SnO_2–BM sample is rutile tetragonal cassiterite, syn, SnO_2 with space group $P4_2/mnm$ having lattice parameters $a = b = 4.735$ Å and $c = 3.165$ Å, and the values could be exactly indexed with standard data, ICDD (PDF-2 Release 2019 RDB) 01-077-0447 (Table S2). However, all three composite architectures exhibited peaks corresponding to both hexagonal graphite and tetragonal SnO_2 with various peak intensities based on the phase composition. The sharp peak at $2\theta = 26.55°$ representing (002) plane of Graphite–BM sample, was shifted to 26.56, 26.58 & 26.59° for C_1, C_2 & C_3 respectively, indicating the overlapping with (110) plane of SnO_2–BM sample at $2\theta = 26.58°$ [40–42]. The crystalline property of all five samples was confirmed by calculating the crystallite size using Scherrer's equation. The crystallite sizes were obtained as 44.99, 56.68, 68.71, 82.87, and 70.37 nm for graphite-BM, C1, C_2, C_3 & SnO_2 -BM samples, respectively (Table S3).

Fig. 1b & Fig. S2 shows Raman spectra of samples. Except for SnO_2 -BM sample, all the samples showed the characteristic peaks at ~1350, ~1600, and ~2700 cm^{-1} corresponding to D, G, and 2D bands of carbonaceous materials, respectively. The G (graphitic) band is due to the in-plane stretching motion (second E_{2g} vibration mode) between sp^2 carbon atoms. The 2D (G') band is a second-order two phonon process and exhibits a strong frequency dependence on excitation laser energy, and is associated with the number of graphene layers. The G band and 2D band together represent the Raman signature of graphitic sp^2 materials. The D band (defect or dispersive band) is generated by out-of-plane vibrations (breathing mode) assigned to the zone center phonons of E_{2g} symmetry and K-point phonons of A_{1g} symmetry. D-band can be

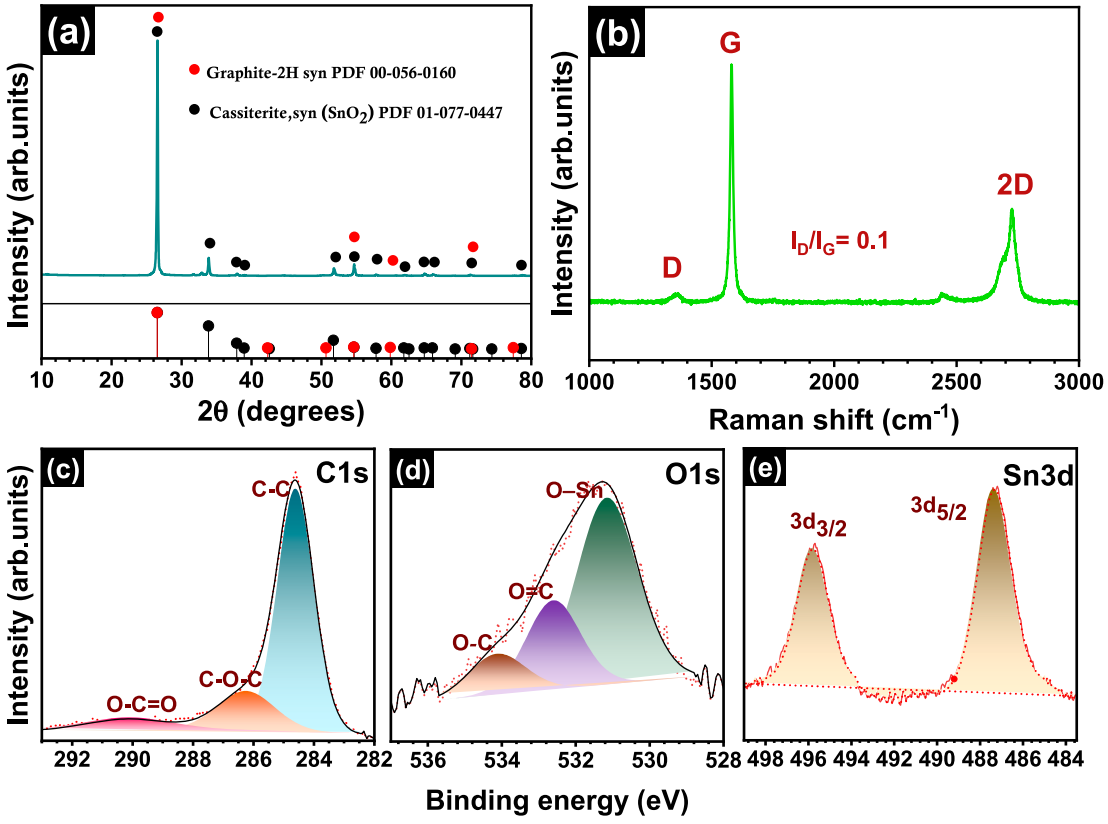

Fig. 1. (a) XRD pattern, (b) Raman spectrum, (c, d & e) deconvoluted XPS spectra of SnO_2 @Graphite nanocomposite (C_1); high resolution spectrum of (c) C1s, (d) O1s, and (e) Sn 3d.

attributed to the presence of structural defects created by ball milling of the sample [43,44]. The intensity ratio of the D band to G-band (I_D/I_G = 0.1) indicates the sample maintains a high degree of graphitization irrespective of the mechanical ball milling procedure [45–51]. The surface chemistry of SnO_2@G *nc* (C_1) was detected by X-ray photoelectron spectroscopy (XPS). Fig. S3 shows the survey spectrum, and it confirms the presence of three main elements carbon (C), oxygen (O), and tin (Sn). The C1s spectrum of carbon can be deconvoluted into three peaks with a maximum binding energy of ~284.55 eV for C–C bond in graphite, ~286.25 eV for C–O groups, and ~290 eV for O–C═O groups, respectively (Fig. 1c). The deconvoluted O1s spectrum, Fig. 1d displays three asymmetrical peaks at binding energy values of ~531, ~532, and ~534 eV corresponding to three chemically non-equivalent states such as O^{2-} ions in SnO_2 lattice, oxygen in O═C bonds, and oxygen in O–C bonds, respectively. The presence of O in O═C bonds and O–C bonds is due to the oxidation of graphite sections that are exposed to air [52]. Fig. 1e illustrates the Sn $3d_{5/2}$ and $3d_{3/2}$ spectra with binding energies ~487 and ~495 eV [53,54].

The surface morphology of SnO_2@G *ncs* and ball-milled samples of Graphite and SnO_2 were observed by field emission scanning electron microscope (FE-SEM), and their images are displayed in Fig. S4. The FE-SEM image of the ball-milled graphite sample shows flaky morphology with a varying size distribution (Fig. S4a). FE-SEM images of SnO_2@G *ncs* illustrate small pieces of bright components adsorbed on the surface of graphite flakes, increasing with the SnO_2 concentration in the nanocomposite (Figs. S4b–d). At the same time, ball-milled SnO_2 exhibits a combination of sheet-like morphology with agglomerated nanoparticles (Fig. S4e). Ball milling could effectively improve the reactivity by reducing the size of particles and consistency of SnO_2 distribution in the nanocomposite [55,56]. Fig. 2a–b shows the FE-SEM images of C_1 nanocomposite in different magnifications. The crystalline structure of the C_1 nanocomposite was further studied by transmission electron microscopy (TEM) analysis. Fig. 2c–e shows TEM images with different magnifications, which clearly indicate the presence of adsorbed SnO_2 nanoparticles on the surface of graphite flakes. The high resolution-TEM (HR-TEM) image (Fig. 2f) clearly presents distinct lattice fringes with different interplanar distances that assure the presence of SnO_2 on the surface of graphite flakes and a high degree of crystallinity of the sample. The selected area electron diffraction (SAED) pattern shows small spots making up concentric circles corresponding to the polycrystallinity of the sample (Fig. 2g). In addition, to further reveal the chemical composition and elemental distribution of SnO_2@G *ncs* (C_1), high-angle annular dark-field scanning transmission electron microscopy (HAADF-STEM) images with energy-dispersive X-ray spectroscopy (EDX) elemental mapping images were recorded and given in Fig. 2 (h–k). Elemental mapping images indicate the presence of elements C, O, and Sn, suggesting the occurrence of SnO_2 particles on the surface of graphite flakes.

3.1. Electrochemical performance analysis

The electrochemical performance of all five material samples was evaluated by cyclic voltammetric (CV) measurements. Fig. 3 illustrates the first two cycles of CV curves measured at a scan rate of 0.1 mV s^{-1} for both the ball-milled graphite, SnO_2 bare sample, and the three SnO_2@G *ncs* samples. Fig. 3a shows the CV profile for the graphite-BM sample. The noticeable cathodic peak observed at 0.7 V *vs.* Li^+/Li in the first cycle corresponds to solid electrolyte interphase (SEI) layer formation. The redox peaks positioned at 0.18 and 0.05 V *vs.* Li^+/Li represent the characteristic LiC_6 formation *via* staging process during the lithiation [57]. The sharp oxidation peak at 0.2 V *vs.* Li^+/Li corresponds to the extraction of Li^+-ions from the binary graphite intercalation compound, LiC_6. In the second cycle, the reduction peak at 0.7 V *vs.* Li^+/Li is disappeared, which shows that the SEI layer inhibits further reduction of electrolytes. Moreover, in the second cycle, there is an increase in peak area corresponding to the de-intercalation of Li-ions, indicating improved Li-ion kinetics and enhanced cyclic efficiency. Nevertheless, ball-milling in the presence of oxygen is demanded to overpower the fracture rate by forming oxides on active centers created during the milling process [58]. Furthermore, the graphite samples are still maintaining the crystallinity as observed from characterization studies. Besides, the stacking defects induced during mechanical agitation can also enhance Li-ion intercalation/de-intercalation kinetics [56,59].

Fig. 3b–d displays the CV profile of SnO_2@G *ncs* samples. The

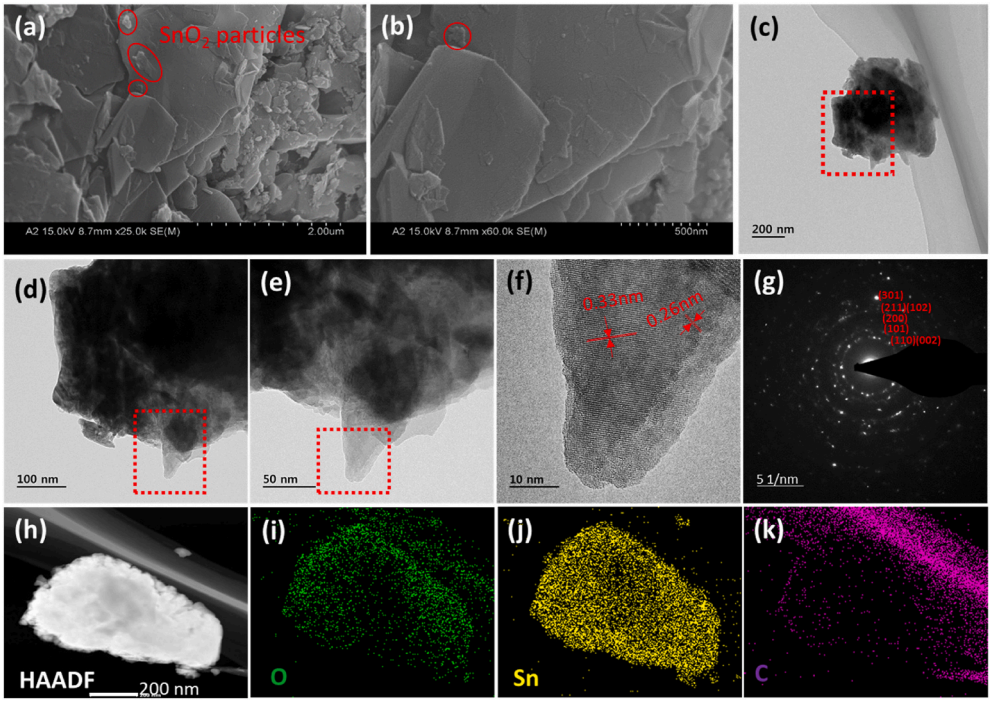

Fig. 2. (a, b) FE-SEM with two different magnifications, (c, d, e) TEM with different magnifications, (f) HR-TEM, (g) SAED pattern; (h) HAADF-STEM images and (i, j & k) EDS mappings of SnO_2 @Graphite nanocomposite (C_1).

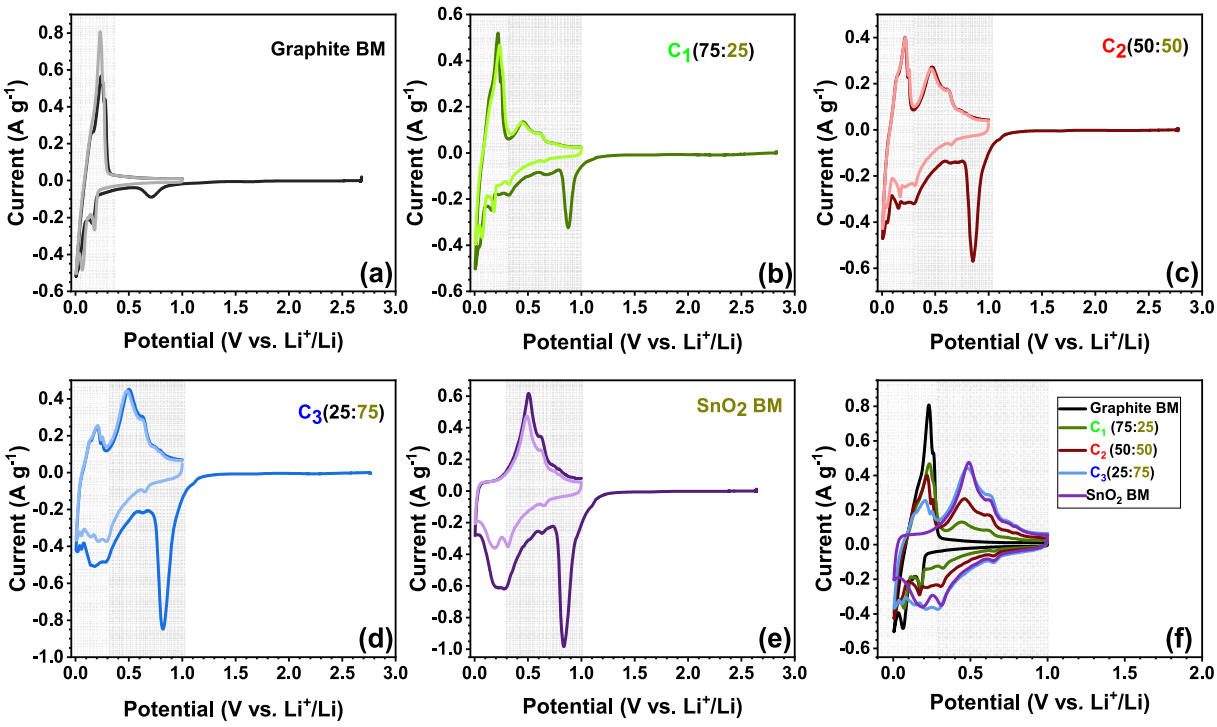

Fig. 3. Cyclic voltammetry profiles (first and second cycle) for SnO_2 @Graphite nanocomposites @0.1 mV s^{-1}; (a) Graphite BM, (b) C_1, (c) C_2, (d) C_3, (e) SnO_2 BM; (f) Comparision of second cycle CV profile for all the five sample. Broadly, blue and pink colour shading represents the insertion/extraction and alloying/de-alloying regions, respectively. (For interpretation of the references to colour in this figure legend, the reader is referred to the Web version of this article.)

prominent reduction peaks at ~0.88, ~0.84, and ~0.82 V *vs.* Li^+/Li for C_1, C_2, and C_3 composites in the first cathodic process correspond to the initial reduction of SnO_2 into $Sn^0 + Li_2O$ (equation (1)), and SEI layer formation originated from electrolyte decomposition [60,61]. These reactions cause a substantial capacity loss during the first cycle, and the peak disappears from the second cycle onwards. There are four other reduction peaks positioned at ~0.6, ~0.3, ~0.1, & ~0.05 V *vs.* Li^+/Li representing alloying (Li_xSn) and intercalation (LiC_6) process during lithiation. The peaks located at ~0.6 and ~0.3 V *vs.* Li^+/Li agree to the multi-step formation of different Li_xSn alloys according to equation (2) [62,63], and the peaks positioned at ~0.1, and ~0.05 V *vs.* Li^+/Li are related to the lithiation of graphite (LiC_6) [61,64]. The oxidation peaks at ~0.2 and ~0.5 V *vs.* Li^+/Li in the following anodic process can be assigned to the de-lithiation potential of graphite and de-alloying of Li_xSn [65,66]. The CV curves remain analogous from the second cycle onwards, indicating good Li-storage reversibility of the composite material [67]. Whereas, moving to the CV curves of C_1 to C_3 composite, a decrease in the intensity of graphite peaks and an increase in the SnO_2 peak intensity could be observed, pointing to the change in composite material composition. For the SnO_2 BM sample, the CV profile exhibits only SnO_2 peaks corresponding to alloying and de-alloying of Sn-metal in the presence of the Li_2O matrix (Fig. 3e). The second cycle CV profile of all the five samples was plotted in Fig. 3f, displaying peak position changes and peak intensity changes for better comparison with variation in peak currents.

Fig. 4a–e shows the galvanostatic discharge-charge profiles for all the five material samples in the first and second cycles. The initial discharge capacities are ~471, ~716, ~868, ~1161, and ~1407 mAh g^{-1} for Graphite BM, C_1, C_2, C_3, and SnO_2 BM samples, respectively, with corresponding initial coulombic efficiencies (CE) of ~70.9, ~56.2, ~49.1, ~45, and ~40.2%. This first cycle capacity loss is mainly attributed to the formation of the SEI layer due to electrolyte decomposition and the initial reduction of SnO_2 to $Sn^0 + Li_2O$. A notable increase in the capacity profiles are noted in the second cycle; accordingly, the half-cells exhibit capacity values of ~353, ~414, ~443, ~548, and ~609 mAh g^{-1} with CE of ~95, ~97, ~95, ~96, and ~92%, respectively. Fig. 4f illustrates the comparison of charge-discharge profiles of all five samples. Apparently, a gradual shifting of intercalation to alloying reaction process is evident in the charge-discharge profiles with an increase in the SnO_2 loading. The obtained galvanostatic profiles match well with the CV traces, in which similar kind behaviors are observed with the appearance of sharp peaks. It is worth mentioning that an increase in the redox potential is noted from graphite to pure SnO_2. Fig. 4g displays the cyclic stability of the materials, and it indicates all the materials exhibit essential stability and decreases with the increasing concentration of SnO_2 in the sample. In addition, it is tough to get data for the SnO_2 BM sample for extended cycling due to the slow kinetics, huge volume variation, and poor performance of the material. This clearly suggests that the presence of graphite not only involves the charge-storage process *via* intercalation and also sustains the volume variation observed during the electrochemical reaction. Further, it is also observed that the redox potential of the reversible lithiation/de-lithiation process is increasing with the rise in SnO_2 composition. Fig. 4h presents the reduction potential of all the material samples in the form of a bar graph which has been calculated based on the intersection of the charge and discharge curves. The obtained redox potential is consistent with the CV and galvanostatic studies.

Fig. S5 presents the rate performance of the materials starting from 0.05 to 2 A g^{-1}. SnO_2@G *ncs* samples exhibit better rate capability in comparison with ball-milled graphite and SnO_2 samples. The C_1 composite shows stable performance at low and high current rates, whereas C_2 and C_3 exhibited poor performance at low current rates. EIS was performed to analyze the electrode/electrolyte interface. Fig. S6 presents the Nyquist plots of SnO_2@G *ncs* and ball-milled samples of bare graphite and SnO_2. The *x*-axis intercept in the high-frequency region represents the bulk resistance (R_1), which is the equivalent series resistance of the current collector, electrolyte, and separator. The R_1 value for all the five half-cell configurations remains between 14 and 18 Ω, representing the same state of charge in all the material electrodes. The term R_2, Q_2 corresponds to Resistance (R_{SEI}) and capacitance of

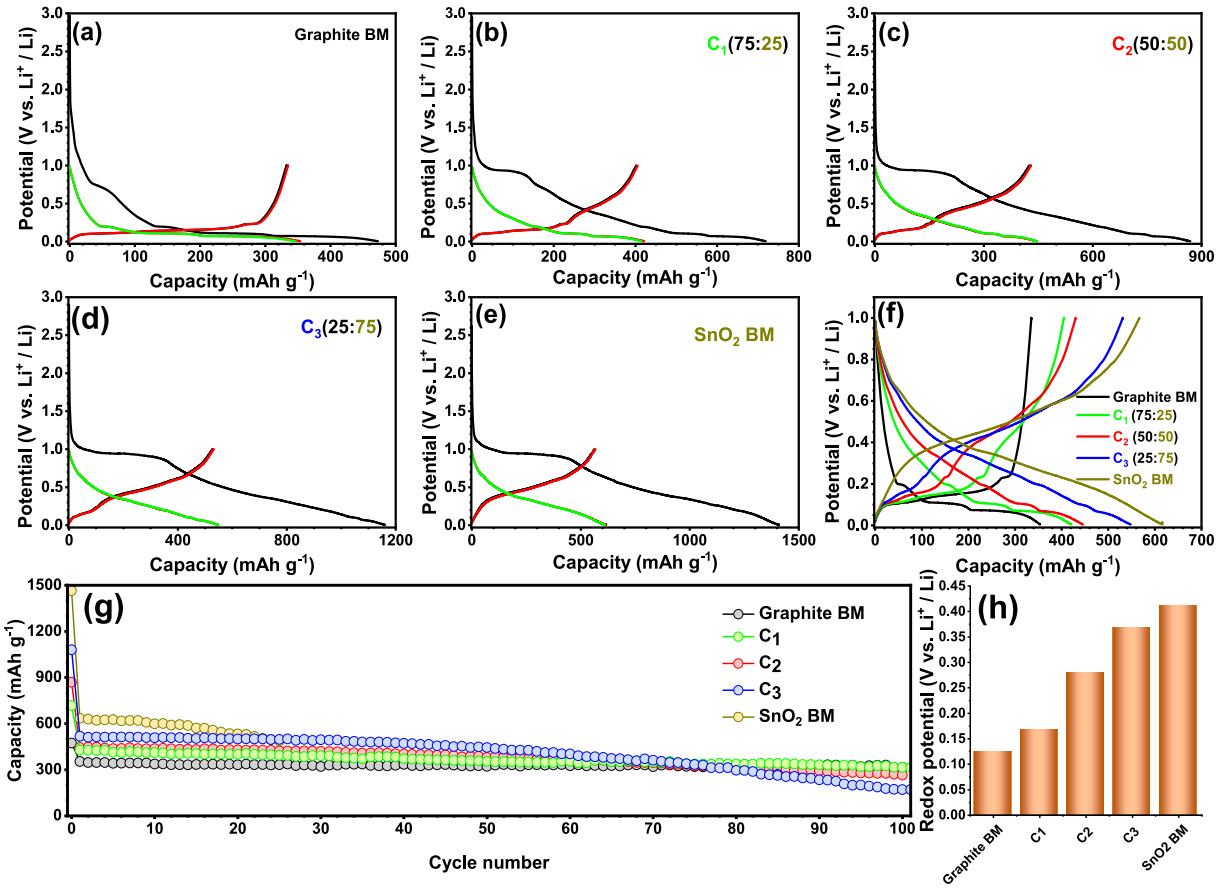

Fig. 4. Galvanostatic charge−discharge profile at a current density of 0.1 A g^{-1} (first & the second cycle) of (a) Graphite BM, (b) C_1, (c) C_2, (d) C_3, (e) SnO_2 BM, (f) Comparison of the second charge-discharge profile of all the five samples, (g) plot of discharge capacity *vs.* cycle number at a current density of 0.1 A g^{-1}, and (h) Comparison of redox potential for SnO_2 @Graphite nanocomposites. The redox potential of the composites has been calculated based on the intersection point of charge and discharge curves (Fig. 4f).

interfacial layer, which are negligible for freshly prepared half–cells. Charge-transfer resistance (R_{CT}) and double-layer capacitance can be indexed with R_3 and Q_3. The R_{CT} of Li-insertion for different material electrodes was observed to be approximately 35, 22, 26, 38, and 27 Ω and can be related to the kinetics of the electrochemical reaction. The final straight line in the low-frequency region is associated with diffusional effects or mass transfer resistance of Li-ions in the electrode materials, which can be analyzed with the value of Warburg impedance (W) [68,69]. The suitability of AC as cathode active material for the assembly of LIC was also tested in half-cell assembly with Li-metal counter electrode under similar testing conditions. Fig. S7a corresponds to the galvanostatic charge-discharge profile for AC *vs.* Li^+/Li electrode. The half–cell delivered an initial specific capacity value of ~86 mAh g^{-1} at a current density of 0.1 A g^{-1}. The long-term cyclic stability of AC half−cell is depicted in Fig. S7b.

3.2. Electrochemical performance of LICs

The assembled LICs with ball-milled samples of graphite, SnO_2, and SnO_2@G *ncs* as the negative electrode material and AC as the positive electrode material in the presence of 1 M $LiPF_6$ electrolyte were tested within the potential window of 1.7–4.2 V. Pre-lithiated negative electrodes (LiC_6 and Li_xSn) were considered to provide enough Li-ions for the reaction upon the wider operating window, and also to improve the initial coloumbic efficiency. The consequence of capacity mismatch in negative and positive electrodes was well-adjusted by AC electrodes with optimum mass ratios [70], Table S4. Fig. 5a–e shows the charge-discharge profile of the assembled AC/Graphite BM, AC/C_1, AC/C_2, AC/C_2, AC/C_3 & AC/SnO_2 BM-based LICs for current rates varying from 0.05 to 1.5 A g^{-1}. It is worth adding that the applied current rates, energy, and power densities are calculated based on the total active mass loading (anode and cathode) of the electrode. The overall reaction mechanism in the LIC device is a cation-anion-consuming process. During charging, PF_6^- ions are adsorbed on the AC electrode, while Li^+ ions get inserted into graphite/SnO_2 anode material by the formation of LiC_6 and Li_xSn alloy. During the period of discharge, both PF_6^- and Li^+ ions move away from AC and graphite BM/SnO_2 BM/SnO_2@G *ncs* electrodes. Thus, the overlapping effect of two different charge storage mechanisms within the single device can be visible from the deviations in the linear charge-discharge profiles with a triangular shape and exhibit small ohmic drops due to the resistivity of assembled LIC devices. However, this LIC configuration is different from the concept of Dual-ion batteries, in which both anion and cations involve in the perfect faradaic reactions [71]. The energy and power density values of assembled LICs were calculated from the galvanostatic profile based on the total mass of active material present in both battery and capacitive type electrodes. These values were illustrated with the help of the Ragone plot given in Fig. 5f. It can be observed that LICs based on SnO_2@G *ncs* electrodes exhibited better performance in comparison with LICs having ball-milled samples of graphite and SnO_2 negative electrode. Among the compositions, the AC/C_1-LIC delivers a high energy density of 172.33 Wh kg^{-1} at a power of 153 W kg^{-1} and maintains 134.12 Wh kg^{-1} even at a high-power density of 4.64 kW kg^{-1}. The AC/C_1-LIC cell renders marginally lower energy than AC/C_3-LIC at low current rates (175.95 Wh kg^{-1}) but displayed excellent performance at higher rates (e.g.,

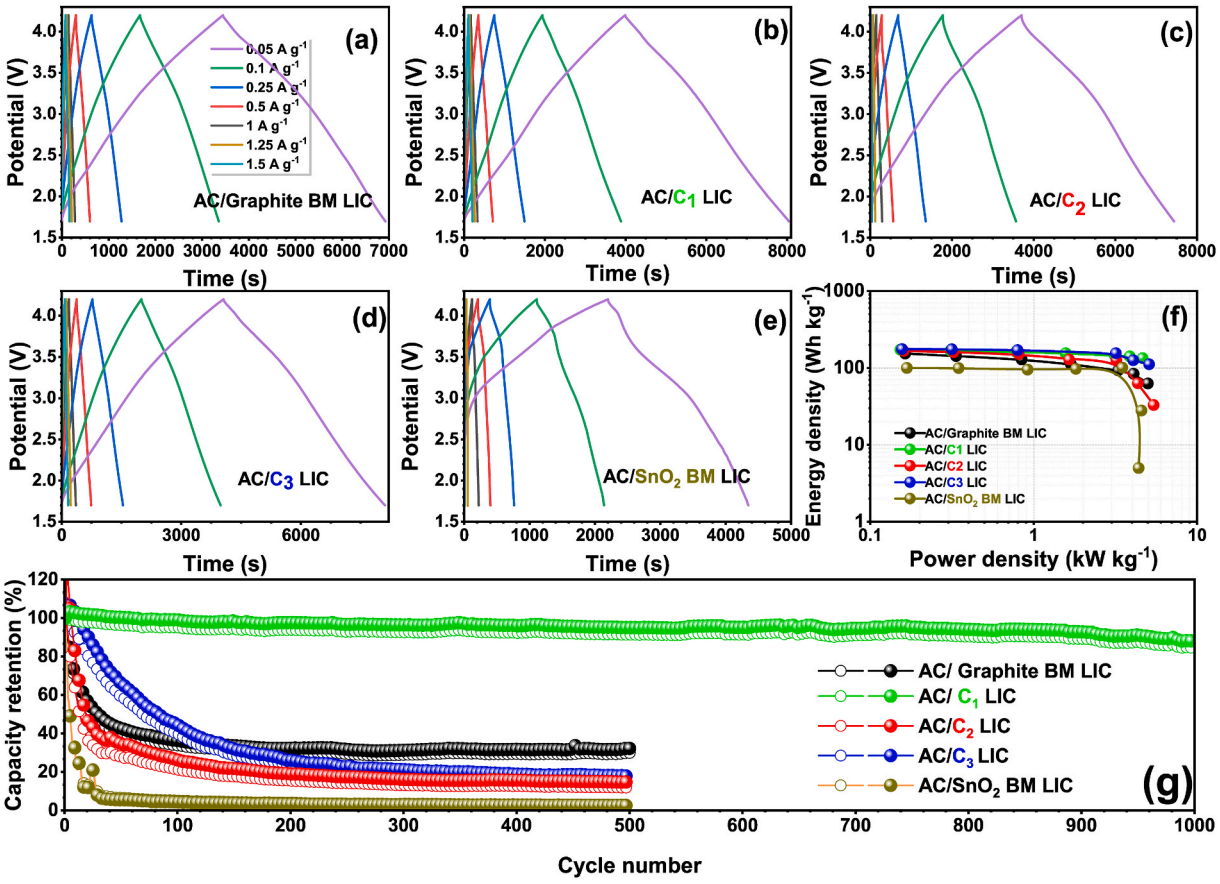

Fig. 5. Electrochemical performance of assembled AC/SnO_2 @Graphite nanocomposite based LICs: (a–e) Galvanostatic charge-discharge profile at various current densities, (a) AC/Graphite BM-LIC, (b) AC/C_1-LIC, (c) AC/C_2-LIC, (d) AC/C_3-LIC, (e) AC/SnO_2 BM-LIC, (f) Ragone plot representation of LICs for energy and power density value comparison, and (g) cyclic stability of assembled LICs. Filled and open symbols correspond to the charge and discharge, respectively.

111.29 Wh kg^{-1} for AC/C_3-LIC). This kind of high energy density LIC, irrespective of the applied current rate, is a mandate for the future requirement. The present study clearly indicates the combination of both alloying and intercalation processes is one of the efficient ways to fulfill future requirements. On the other hand, the AC/C_2-LIC and AC/graphite–BM-LIC shows decent energy density values of 166.04 and 153.74 Wh kg^{-1}, respectively, which are superior to AC/SnO_2 BM-based LIC (99.95 Wh kg^{-1}). Overall, the synergistic effect of the intercalation and alloying process certainly elevates the electrochemical performance of the LICs.

Fig. 5g shows the long-term cyclability of the LICs mentioned above. It was observed that except for the LIC with C_1 composite negative electrode, all other LICs suffered a drastic capacity reduction during the initial cycles. After ~200 charge-discharge cycles, they could show a stable performance with reduced capacity values. At the same time, AC/C_1 LIC could deliver a steady performance such that even after a 1000 charge-discharge cycle, the LIC could maintain 84.5% of the initial capacity. The study revealed that SnO_2@G *ncs* based LICs with tailored composition could establish more energy storage capability than bare graphite samples by incorporating alloying mechanism along with intercalation chemistry. Besides, the best SnO_2@G *ncs*, C_1 based LIC could exhibit cyclic stability along with high energy and power density values. Thus, the loading value of SnO_2 should be optimum such that a high loading of SnO_2 could block the channels of ionic diffusion. The ionic diffusion speed and SnO_2 loading should be balanced to obtain a LIC with high energy density, fast kinetics, and long-term durability. After 1000 charge-discharge cycles, the AC/C_1 LIC was also placed at constant high and low-temperature conditions (10, 5, 50 & 25 °C) with the help of an environmental chamber to test its performance. Fig. 6a–d illustrates the charge-discharge profile at different temperature conditions. The near-linear charge-discharge profile of the device at all temperature conditions indicates its wide temperature range of operational stability. A decrease in charge-discharge time at high temperatures indicates the fast kinetics at high-temperature conditions. The device could deliver maximum energy density values of ~152, ~157, ~135, and ~121 Wh kg^{-1} at 50, 25, 10 and −5 °C, respectively (Fig. 6e). Fig. 6f shows the CV profile of assembled AC/C_1 LIC at different scan rates. The distorted rectangular CV profiles ensure the presence of a hybrid charge mechanism within the LIC device. Moreover, the device could maintain ~96, ~86, ~84, and ~62% of initial capacity after 1000 charge-discharge cycles (Fig. 6g). A duplicate cell was placed on studying the long-term durability of such a fascinating configuration at the ambient condition; the AC/C_1 LIC could be able to operate with ~90% initial capacity at the applied current density of 1 A g^{-1} after undergoing 9000 charge-discharge cycles, Fig. S8. Table S5 summarises the performance of assembled LICs at a current density of 1 A g^{-1}.

The Nyquist plots for AC/C_1 LIC device before and after cycling is illustrated in Fig. S9. Semicircles in the high-frequency regions for the plots after cycling indicate R_{CT} resistance caused by the migration of ions through the resistive element, SEI layer on the negative surface electrode. Slightly increased values of solution resistance (R_s) and R_{CT} for the cycled LIC compared with fresh LIC indicate good compatibility of the system. Therefore, this device can be considered as an ideal LIC with high energy, high power, and long-term stability. Besides, the device can be fully charged and discharged within ~3 min with a current input of 1 A g^{-1}. Furthermore, this report also shows the possibility of incorporating alloying mechanism and intercalation to fabricate high-performance lithium-ion capacitors. These results are much better in

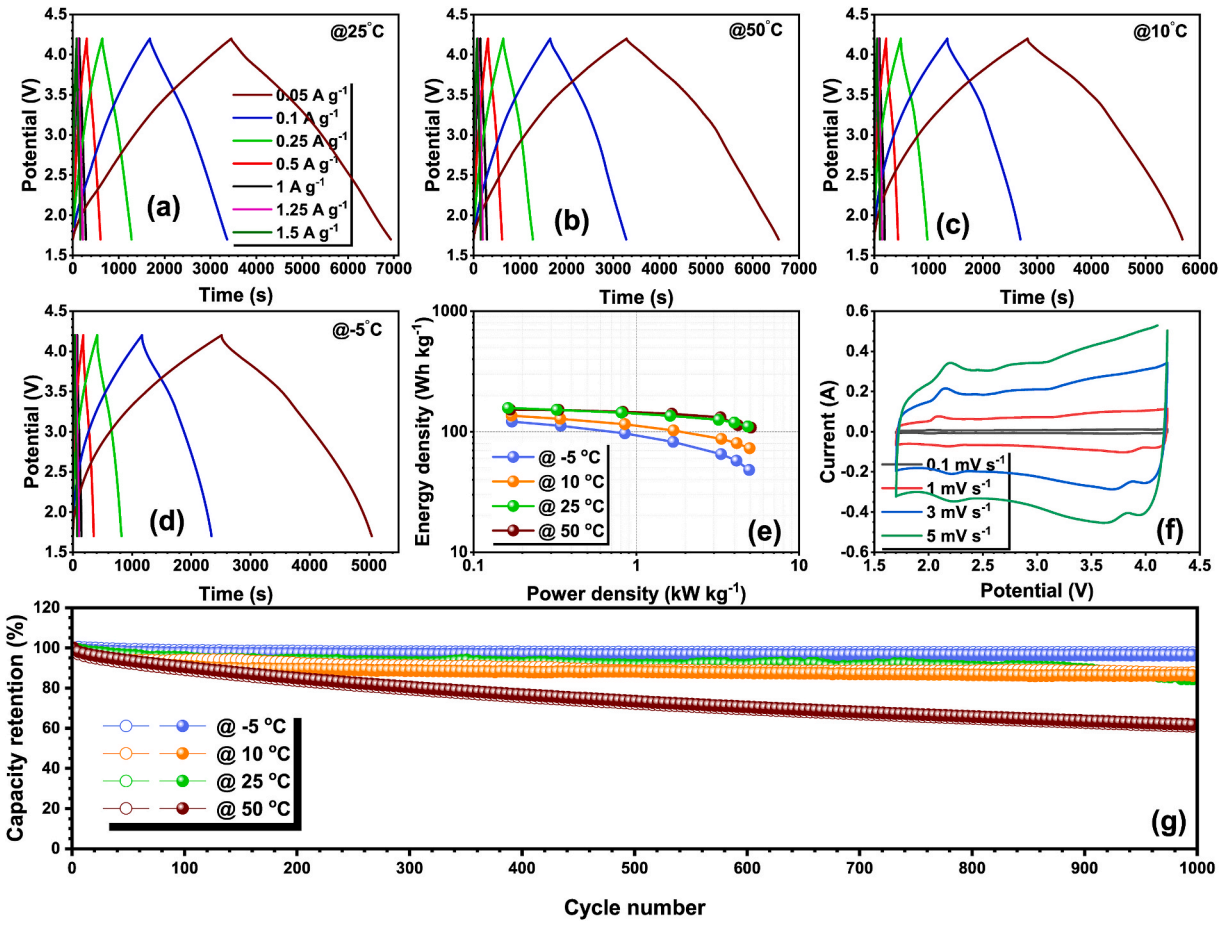

Fig. 6. Performance of AC/C_1-LIC: (a–d) Typical galvanostatic charge-discharge profile at various temperature conditions, (e) Ragone plot representing energy and power density values, (f) Cyclic voltammetry profile at different scan rates recorded at 25 °C, and (g) long-term cycling stability at a current density of 1 A g^{-1} at various temperature conditions. Filled and open symbols correspond to the charge and discharge, respectively.

comparison with the state of art reports for LIC systems based on Sn-derivatives (Table S6). However, in the reported Sn-based systems, mostly amorphous carbon is used to formulate the composite, which sustains the huge volume variation observed during alloying/de-alloying process. But in the present case, we have used graphite as a carbonaceous component which not only acts as a buffer to sustain the volume variation and also involves highly reversible Li-storage with lower redox potential. This SnO_2@Graphite composite is completely unique, which is not only useful for the negative electrode for the development of next-generation LICs and can certainly be extended for the LIB applications as a promising high-capacity anode.

4. Conclusion

In summary, we have designed a new LIC system by pairing battery type SnO_2@G *ncs* negative electrode with a capacitor type commercial AC positive electrode. SnO_2@G *ncs* were synthesized by mechanical ball milling of hydrothermally synthesized SnO_2 with commercial graphite powder. The AC/C_1-based LIC delivered a maximum energy density of 172.33 Wh kg^{-1} at a power of 153 W kg^{-1} in ambient temperature conditions with retention of over 90% capacity after 9000 cycles. We strongly believe that the synergy between the lithiated phases, Li_xSn and LiC_6, is one of the prime factors for such high-performance LICs. Also, the feasibility of using such fascinating LIC in different temperature conditions was evaluated, and it was found that lowering the temperature leads to a highly stable performance. The results clearly illustrate that the combination of both Li-storage mechanisms benefits the development of battery-type electrodes for LIC applications. In addition, such alloying-intercalation-based composites with lower redox potentials can be efficiently used as anode for LIB perspective as well. Overall, the results are remarkable. This study paves the way for incorporating alloy-type materials into intercalation-based anodes to explore electrochemical energy storage devices, *i.e.*, Li-ion capacitors or Li-ion batteries with high energy and high power.

Author statement

MLD, and VA is responsible for Conceptualization, MLD and SP for investigation, MLD, SP, YSL and VA for Writing - Review & Editing, and MLD, YSL and VA for Funding acquisition.

Data availability statement

The data will be made available with the reasonable request to the corresponding author.

Declaration of competing interest

The authors declare that they have no known competing financial interests or personal relationships that could have appeared to influence the work reported in this paper.

Acknowledgments

MLD wishes to thank the funding through Women Scientist Scheme-B (DST/WOS-B/2018/2039) from the KIRAN division of the Department

of Science & Technology (DST), Govt. of India. YSL acknowledges the financial support from the National Research Foundation of Korea (NRF) grant funded by the Korean government (Ministry of Science, ICT & Future Planning) (No. 2019R1A4A2001527). VA acknowledges financial support from the Science and Engineering Research Board (SERB) through Start-up Research Grant (SRG/2020/000002) and DST for Swarnajayanti Fellowship (DST/SJF/PSA-02/2019–20).

Appendix A. Supplementary data

Supplementary data to this article can be found online at https://doi.org/10.1016/j.compositesb.2021.109487.

References

[1] Al Shaqsi AZ, Sopian K, Al-Hinai A. Energy Rep 2020;6:288–306.
[2] Sakai M, Amano M. Hitachi chemical technical report. 2013. p. 9–11.
[3] Whittingham MS. Proc IEEE 2012;100:1518–34.
[4] Hadjipaschalis I, Poullikkas A, Efthimiou V. Renew Sustain Energy Rev 2009;13:1513–22.
[5] Ibrahim H, Ilinca A, Perron J. Renew Sustain Energy Rev 2008;12:1221–50.
[6] Hall PJ, Bain EJ. Energy Pol 2008;36:4352–5.
[7] Oswal M, Paul J, Zhao R. USA: University of Southen California; 2010.
[8] Bourzac K. Nature 2015;526. S105-S105.
[9] Turcheniuk K, Bondarev D, Singhal V, Yushin G. Nature Publishing Group; 2018.
[10] Lei T, Hu Y, Chen W, Lv W, Jiao Y, Wang X, Lv X, Yan Y, Huang J, Chu J, Yan C, Wu C, Wang X, He W, Xiong J. Energy Storage Mater. 2020;26:65–72.
[11] Xue L, Zeng L, Kang W, Chen H, Hu Y, Li Y, Chen W, Lei T, Yan Y, Yang C, Hu A, Wang X, Xiong J, Zhang C. Adv Energy Mater 2021;11:2100420.
[12] Choi NS, Chen Z, Freunberger SA, Ji X, Sun YK, Amine K, Yushin G, Nazar LF, Cho J, Bruce PG. Angew Chem Int Ed 2012;51:9994–10024.
[13] Sharma P, Bhatti TS. Energy Convers Manag 2010;51:2901–12.
[14] Ding J, Hu W, Paek E, Mitlin D. Chem Rev 2018;118:6457–98.
[15] Soltani M, Beheshti SH. J Energy Storage 2020:102019.
[16] Zou K, Cai P, Cao X, Zou G, Hou H, Ji X. Curr Opin Electrochem 2020;21:31–9.
[17] J. Ronsmans, B. Lalande, in, IEEE, pp. 1-4.
[18] Chu A, Braatz P. J Power Sources 2002;112:236–46.
[19] Wang H, Zhu C, Chao D, Yan Q, Fan HJ. Adv Mater 2017;29:1702093.
[20] Han P, Xu G, Han X, Zhao J, Zhou X, Cui G. Adv Energy Mater 2018;8:1801243.
[21] Kularatna N, Gunawardane K. Energy storage devices for electronic systems: rechargeable batteries and supercapacitors. Academic Press; 2021.
[22] Omar N, Ronsmans J, Firozu Y, Monem MA, Samba A, Gualous H, Hegazy O, Smekens J, Coosemans T, Bossche PVd, Mierlo JV. In: 2013 world electric vehicle symposium and exhibition (EVS27); 2013. p. 1–11.
[23] Divya ML, Aravindan V. Chem Asian J 2019;14:4665–72.
[24] Li G, Yang Z, Yin Z, Guo H, Wang Z, Yan G, Liu Y, Li L, Wang J. J Mater Chem 2019;7:15541–63.
[25] Divya ML, Natarajan S, Lee Y-S, Aravindan V. J Mater Chem 2020;8:4950–9.
[26] Sennu P, Arun N, Madhavi S, Aravindan V, Lee Y-S. J Power Sources 2019;414:96–102.
[27] Hassan AS, Moyer K, Ramachandran BR, Wick CD. J Phys Chem C 2016;120:2036–46.
[28] Aravindan V, Jinesh KB, Prabhakar RR, Kale VS, Madhavi S. Nanomater Energy 2013;2:720–5.
[29] Aravindan V, Sundaramurthy J, Kumar EN, Kumar PS, Ling WC, von Hagen R, Mathur S, Ramakrishna S, Madhavi S. Electrochim Acta 2014;121:109–15.
[30] Zhao S, Sewell CD, Liu R, Jia S, Wang Z, He Y, Yuan K, Jin H, Wang S, Liu X, Lin Z. Adv Energy Mater 2020;10:1902657.
[31] Zhou X, Wan L-J, Guo Y-G. Adv Mater 2013;25:2152–7.
[32] Aravindan V, Lee YS, Madhavi S. Adv Energy Mater 2015;5:1402225.
[33] Read J, Foster D, Wolfenstine J, Behl W. J Power Sources 2001;96:277–81.
[34] Qu W-H, Han F, Lu A-H, Xing C, Qiao M, Li W-C. J Mater Chem 2014;2:6549–57.
[35] Sun F, Gao J, Zhu Y, Pi X, Wang L, Liu X, Qin Y. Sci Rep 2017;7:40990.
[36] Sennu P, Aravindan V, Lee Y-S. Chem Eng J 2017;324:26–34.
[37] Xuan Tran M, Kim AY, Lee JK. Appl Surf Sci 2018;461:161–70.
[38] Arnaiz M, Botas C, Carriazo D, Mysyk R, Mijangos F, Rojo T, Ajuria J, Goikolea E. Electrochim Acta 2018;284:542–50.
[39] Lei T, Chen W, Lv W, Huang J, Zhu J, Chu J, Yan C, Wu C, Yan Y, He W, Xiong J, Li Y, Yan C, Goodenough JB, Duan X. Joule 2018;2:2091–104.
[40] Wang Y, Lee JY. J Power Sources 2005;144:220–5.
[41] Gu F, Fen Wang S, Feng Song C, Kai Lü M, Xin Qi Y, Jun Zhou G, Xu D, Rong Yuan D. Chem Phys Lett 2003;372:451–4.
[42] Liu H, Huang J, Li X, Liu J, Zhang Y. Ceram Int 2012;38:5145–9.
[43] Bokobza L, Bruneel J-L, Couzi M. Chimia 2015:1.
[44] Merlen A, Buijnsters JG, Pardanaud C. Chapter 13 Raman spectroscopy characterization of carbon materials: from graphene to all-carbon heterostructures. In: All-carbon composites and hybrids. The Royal Society of Chemistry; 2021. p. 317–46.
[45] Sun X. Ionics 2020;26:3841–51.
[46] Angoni K. Carbon 1993;31:537–47.
[47] Leon V, Quintana M, Herrero MA, Fierro JLG, de la Hoz A, Prato M, Vazquez E. Chem Commun 2011;47:10936–8.
[48] Dennison JR, Holtz M, Swain G. Spectroscopy 1996:11.
[49] Wang J, Ciucci F. Appl Catal B Environ 2019;254:292–9.
[50] Wang J, Kong H, Zhang J, Hao Y, Shao Z, Ciucci F. Prog Mater Sci 2021;116:100717.
[51] Wang J, Kim J, Choi S, Wang H, Lim J. Small Methods 2020;4:2000621.
[52] Blyth RIR, Buqa H, Netzer FP, Ramsey MG, Besenhard JO, Golob P, Winter M. Appl Surf Sci 2000;167:99–106.
[53] Rong X, Chen D, Qu G, Li T, Zhang R, Sun J. Sensor Actuator B Chem 2018;269:223–37.
[54] Stranick MA, Moskwa A. Surf Sci Spectra 1993;2:50–4.
[55] Song J-S, Cho G-B, Kim K-W, Ahn H-J, Kim H-S, Ahn J-H, Cho K-K. Appl Surf Sci 2019;481:736–40.
[56] Jung D-W, Jeong J-H, Cha B-C, Kim J-B, Kong B-S, Lee JK, Oh E-S. Met Mater Int 2011;17:1021–6.
[57] Ding Z, Li X, Wei T, Yin Z, Li X. Electrochim Acta 2016;196:622–8.
[58] Šepelák V, Bégin-Colin S, Le Caër G. Dalton Trans 2012;41:11927–48.
[59] Sivakkumar SR, Milev AS, Pandolfo AG. Electrochim Acta 2011;56:9700–6.
[60] Liu X, Han Y, Zeng J, Yang H, Zhou K, Pan D. J Mater Sci Mater Electron 2018;29:5710–7.
[61] Xie Q, Zhu Y, Zhao P, Zhang Y, Wu S. J Mater Sci 2018;53:9206–16.
[62] Birrozzi A, Asenbauer J, Ashton TE, Groves AR, Geiger D, Kaiser U, Darr JA, Bresser D. Batter Supercaps 2020;3:284–92.
[63] Ma Y, Ma Y, Giuli G, Diemant T, Behm RJ, Geiger D, Kaiser U, Ulissi U, Passerini S, Bresser D. Sustain Energy Fuel 2018;2:2601–8.
[64] Liu Q, Li S, Wang S, Zhang X, Zhou S, Bai Y, Zheng J, Lu X. J Phys Chem Lett 2018;9:5567–73.
[65] Ambalkar AA, Panmand RP, Kawade UV, Sethi YA, Naik SD, Kulkarni MV, Adhyapak PV, Kale BB. New J Chem 2020;44:3366–74.
[66] Yi L, Liu L, Guo G, Chen X, Zhang Y, Yu S, Wang X. Electrochim Acta 2017;240:63–71.
[67] Ng V, Wu S, Liu P, Zhu B, Yu L, Wang C, Huang H, Xu Z, Yao Z, Zhou J, Que W, Kong L. Electrochim Acta 2017;248:440–8.
[68] Middlemiss LA, Rennie AJR, Sayers R, West AR. Energy Rep 2020;6:232–41.
[69] Choi W, Shin H-C, Kim JM, Choi J-Y, Yoon W-S. J Electrochem Sci Technol 2020;11:1–13.
[70] Panja T, Ajuria J, Díez N, Bhattacharjya D, Goikolea E, Carriazo D. Sci Rep 2020;10:10842.
[71] Sui Y, Liu C, Masse RC, Neale ZG, Atif M, AlSalhi M, Cao G. Energy Storage Mater. 2020;25:1–32.